

Computational Fluid Dynamics and Experimental Hydrodynamic Analysis of a Solar AUV

Ehsan ASADI ASRAMI¹*, Mohammad MOONESUN²,
Farhad AZIZI ABI³)

¹) *Takestan Islamic Azad University
Energy Conversion Department*

5 km of Hamedan road, Takestan, Qazvin, Iran

*Corresponding Author e-mail: easadiasrami@gmail.com

²) *Malek-e-Ashtar University of Technology
Faculty of Naval Architecture and Marine Engineering*

Ferdowsi Blvd, Sahinshahr, Iran

e-mail: m.moonesun@gmail.com

³) *Sharif University of Technology
Department of Mechanical Engineering*

Azadi Street, Tehran, Iran

e-mail: kakhoda53far@gmail.com

In the present study, the effect of free surface on the hydrodynamic forces acting on the motion of an autonomous underwater vehicle (AUV) has been investigated. The AUV is powered by solar energy. Using computational fluid dynamics, the Reynolds averaged Navier Stokes (RANS) equations for the flow around the AUV are solved, and the free surface effect is simulated using the volume of fluid (VOF) two-phase flow model. For this purpose, the commercial code ANSYS FLUENT 18 was used [1]. The results of the numerical solution are compared with experimental results of the AUV model in the surface motion in the towing tank of the Persian Gulf National Laboratory with a scale of 1:1. The experiment was performed in a fixed draft and the velocity was ranging from 0.2 m/s to 1.4 m/s (according to Reynolds number 2.4×10^5 to 1.7×10^6).

Keywords: solar AUV, free surface, CFD, towing tank.

1. INTRODUCTION

Submarines behave in a surface motion similar to ships that move on the water. The surface movement resistance of a submarine is greater than its underwater motion when advance velocity is not low. This is because, in surface

motion, the vessel experiences wave resistance, and the phenomena of fluid flow movement around it are quite different from those during the underwater motion. Although submarines are designed to move underwater, they have to rise to the surface to carry out various missions. Especially, for an AUV that takes the required energy from the Sun, it is necessary to get to the surface. Therefore, hydrodynamic analysis of the surface motion of such an AUV is essential. The most important forces acting on a submarine body are the skin friction drag and the residual drag. The skin frictional drag is created by the shear stress due to viscosity, and the residual drag by the phenomenon of wave-making and shape drag. In fully submerged AUV motion, the vessel's total drag depends on the water viscosity, the vessel's shape and its speed. However, in surface motion, wave-making resistance has a large share in total resistance. To study the hydrodynamic performance of the underwater vehicle, the equations governing the flow around the vessel must be solved. Relevant hydrodynamic coefficients must also be calculated to obtain the hydrodynamic forces acting on the underwater vehicle. When the CFD (computational fluid dynamics) method is implemented, it is common to define a solution domain for the vehicle model after sketching it and also determine the boundary conditions for that solution domain. Then, by meshing the solution domain in a way that fits the problem, we can solve the equations governing the flow within that domain. By solving the equations of continuity and momentum simultaneously, the hydrodynamic coefficients can be derived. The effect of the free surface is also simulated by solving the VOF equation. In this investigation, to obtain the hydrodynamic forces acting on the AUV body in the experimental test, an AUV model has been constructed. The surface of the body was polished and painted (Fig. 3) to provide a minimum roughness according to the International Towing Tank Conference (ITTC) standard procedure 7.5-02-03-01.4 (revision 04-2017), and it has been tested at one of ITTC's approved towing tanks at different speeds. In this experiment, the axial force on the vessel is measured at any speed. If the model is made on a scale from the original sample, the coefficients obtained from the model test should be generalized to the main body using analogy relationships.

In numerical studies of AUV's hydrodynamics, De Marco *et al.* [2] presented experimental and numerical hydrodynamic analysis of a stepped planing hull. The experiments were carried out in a towing tank and water was considered calm. The down-thrust methodology with a towed point located in the hull bow was used and numerical experiments made via RANS and Large Eddy Simulations (LES), with different moving mesh techniques (over-set/chimera and morphing grid), were performed at different model speeds. The flow patterns obtained numerically through LES on a refined grid appear similar to those observed in towing tank investigations through photographic acquisitions.

Javadi *et al.* [3] conducted an experimental study of the AUV bow shape's effect on resistance to an AUV movement in surface motion. Two different bow shapes: tango and standard shape were used. The generated wave field was analyzed around two bodies. The range of analyzed Froude numbers varied from 0.099 to 0.349, and in this range, total, residual and frictional resistances were obtained. The results showed that in the Froude number range of 0.19 to 0.3, the residual drag of the standard bow shape was greater than that of the tango.

Rhee *et al.* [4] studied a mathematical model of wave forces for the depth control of a submerged body near the free surface. First, they designed a mathematical model to calculate the wave forces acting on a submerged body, which was based on the wave exciting forces and moments acting on a square pillar. Next, the effect of the free surface acting on the body was considered. Finally, a mathematical model for control surfaces was proposed, which took into account the effect of the free surface and the wave rotational motions of fluid particles. During this process, a control system was designed to maintain a constant depth below average sea level and minimize pitch angles.

Mansoorzadeh and Javanmard [5] investigated the effects of free surface on drag and lift coefficients for an AUV using experimental and CFD methods. They compared the numerical solution results to obtain the drag and lift coefficients with the experimental results obtained from testing a model with a scale of 1:1. The test depths ranges for the model varied from 0.87 to 5.22 of the AUV maximum diameter and the study was conducted at two speeds of 1.5 m/s and 2.5 m/s. The changes in the drag and lift coefficients at different depths for these two velocities are shown in their paper.

Moonesun *et al.* [6] presented the technical notes on experiments of a fully-submerged submarine model near the water surface. The authors tested a bare hull model in a towing tank at snorkel depth. The draft was considered as the submarine maximum mid-section diameter. Since the induced struts drag is an important challenge, they performed the estimation of one kind of a strut and the interaction between struts and bare hull by considering the free surface effect and each component individually. The results were obtained by both numerical and experimental methods and were compared. The FLOW-3D (V.10) was used as a CFD tool, and also the VOF two-phase model was solved.

Dalayeli *et al.* [7] investigated the wave profile and deck wetness of a submarine moving on the water surface. The authors analyzed two different bow shapes: standard Defence Research Establishment Atlantic (DREA) and tango, by two methods: CFD and experimental method. Experiments were conducted in the towing tank of Isfahan University of Technology (IUT) and the analysis was performed for a bare hull model at two different drafts by using Flow Vision (V.2.3) software. They modeled the wave profile and calculated added resistance and bow wetness for both bow shapes.

Moonesun *et al.* [8] studied the wave-making system in a submarine at surface condition and evaluated the critical Froude numbers of the wave-making system. Also, they focused on the hump and hollow profiles according to Froude numbers and the range of a maximum of this number was obtained statistically by using three methods: CFD, experimental method and analytical formulas. The CFD analysis for the bare hull was performed using Flow Vision (V.2.3) as a CFD tool, and experiments were conducted in the towing tank of Isfahan University of Technology (IUT). Moonesun *et al.* [9] evaluated the effective depth of regular wave on submerged submarines and AUVs. They recommended a safe and calm depth called the “wave base” and showed that it could be 0.1λ . They concluded that by increasing the depth the submarine motion drag reduced. In their study, Flow-3D (V.10) was employed as CFD commercial code.

Nematollahi *et al.* [10] investigated numerically the interaction of a symmetrical AUV with a free surface. The turbulence model used was the $k-\epsilon$ model, and the free surface simulation method used was the VOF method. The study was performed at different Reynolds numbers at different depths and the flow wake behind the vessel was analyzed. They reported that for a fixed Reynolds number, the pressure drag as well as the coefficient of resistance increase with decreasing Froude number, and for the Reynolds number of $H \geq 3$ (dimensionless depth), the free surface effect can be neglected. Also, at low immersion depths, the effect of the UWV (underwater vehicle) movement on the free surface becomes more significant if the Reynolds value increases.

Razgallah *et al.* [11] investigated, by varying the depth of water, drift angle and ship speed in inland waterways, the impact of free surface modeling on hydrodynamic forces for ship navigating. Their work focused on the investigation of the importance of free surface assessment on the estimation of the hydrodynamic forces, particularly in the presence of the ship–bottom interaction and when certain parameters are varied, including the ship’s speed and the drift angle. Numerical code under the commercial software Ansys Fluent was used by solving Reynolds-averaged Navier–Stokes equations (RANSE) coupled to a $k-\omega$ SST turbulence model. To investigate the effect of free surface modeling, the hydrodynamic forces were compared when the free surface separating air and water was considered, using the VOF method, and when the free surface is neglected.

Salari and Rava [12] tested the hydrodynamics of the flow on the body of an AUV in the vicinity of the free surface, considering the transition from laminar to turbulent flow. They obtained the hydrodynamic coefficients of an AUV at 0.75, 1, 1.5, 2, and 4D (according to maximum diameter) at a near-free surface. RANS equations were discretized using finite volume methods and the free surface was simulated with the VOF model. Since the AUV’s speed was slow, the effect of the boundary layer transition from laminar to turbulent was considered. They considered two modes of turbulence, one for the fully turbulent mode using the

$k-\varepsilon$ model and the other for the turbulent transitional mode using the Menter's transition – SST model. The results showed that the Menter's transition – SST model is closer to the laboratory data. Also, the wave-making effects were studied at different immersion depths in the sea-surface vicinity or at finite depths. It has also been observed that in the straight-line movement of this vessel with the symmetrical body of the axis due to the movement in the vicinity of the free surface, the coefficients of lift and pitch moments are not zero. However, for greater depths, this is not to be expected.

Shariati and Mousavizadegan [13], regarding appendages of submersible vehicles near the free surface, employed CFD to evaluate the increase of vehicle body resistance which in this study was the DARPA SUBOFF model. They concluded that appendages do not have strong effect on wave-making resistance and wave pattern generated by the vehicle body. This resistance can comprise only 14.5–22.3% of the total resistance. In addition, appendages can strongly affect pressure viscous resistance. Steenson *et al.* [14] analyzed the performance of an AUV that moves with vertical tunnel thrusters near the surface in waves. They have shown that when the vertical thruster moves toward the free surface, the generated thrust is reduced. The experimental results showing the above results are presented and discussed. The Delphin2 AUV was also tested in motion between the waves, and suggestions were presented for its optimization.

In the present study, a solar AUV model with a scale of 1:1 with a length of 1.2 m and an L/D ratio of 8.6 was tested in the towing tank of the National Iranian Marine Laboratory (NIMALA). This Solar AUV has been investigated to assess the capability of photovoltaic panels to provide the required thrust power. Figure 1 illustrates the main dimensions of the AUV body. The model under the study consists of two large wings with a cross-sectional area based on NACA0015 so that the photovoltaic panel can be installed on it. The upper surface of the wings is cut along the length. This creates a 2° upward angle with respect to the body longitudinal centerline and, therefore, the wing is not symmetrical. Also, four hydroplanes with the same cross-section are installed at the end of the vessel with an angle of 90° to each other – two for the rudders and two for the end hydroplanes. The AUV's midsection is the DARPA SUBOFF model, which can be seen in the figure below.

Note that the end parts of rudders and wings, which are shown in Fig. 1, are placed inside the mid-body. By using ANSYS FLUENT 18 software, the RANS equations around the AUV body are solved in the specified range, and the determined inputs are defined in the boundary conditions, and the two-phase flow is solved by the VOF method. The turbulence model used is the $k-\varepsilon$ standard model. The drag and lift coefficients for the Froude number range from 0.0583 to 0.408. The wave pattern on the body and its surroundings are obtained and compared with experimental data.

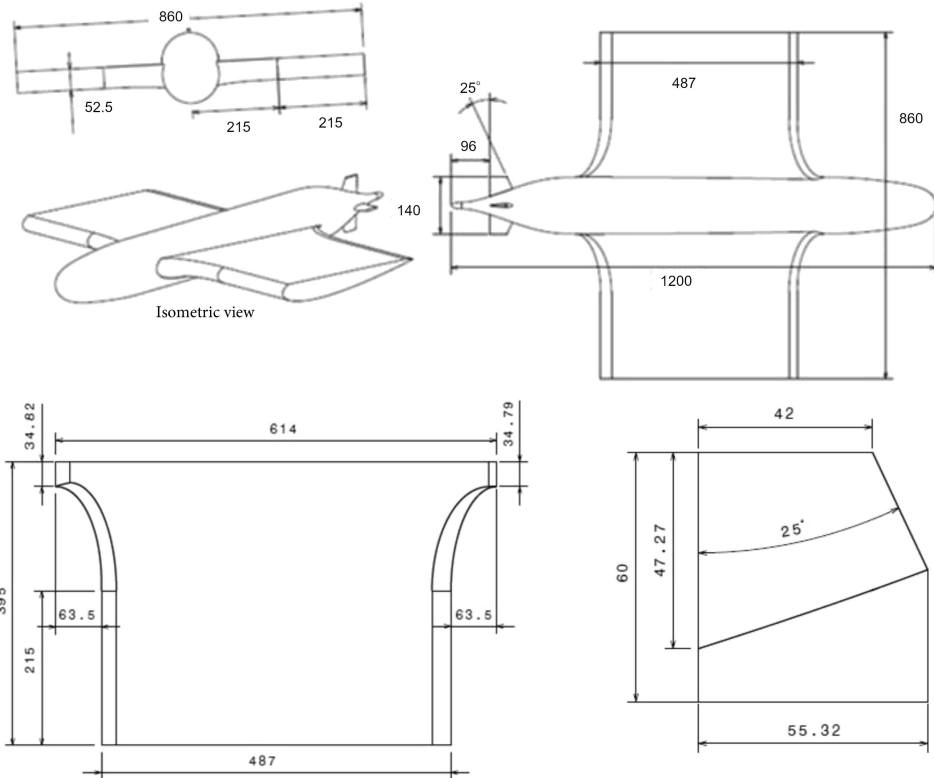


FIG. 1. The main dimensions of the studied solar AUV in millimeters, total body, large wing and rudder.

TABLE 1. Main dimensions of solar AUV in millimeters.

AUV components	Dimensions [mm]
Overall length	1200
Width	860
Midbody section maximum diameter	140
Wing root chord length	614
Wingtip chord length	487
Wing camber thickness	52.66
Rudder root chord length	55.32
Rudder tip chord length	42
Rudder camber thickness	6.3

2. EXPERIMENTAL SETUP

A 1:1 scale model was constructed by the researchers using Abies wood and tested in the towing tank of the National Iranian Marine Laboratory. The di-

mensions of the towing tank (shown in Fig. 2) are 402 m in length, 6 m in width, and 4.5 m in depth. The carriage is a crew type with a capacity of 5 people with dimensions of 7.6×7 m. Its low-speed motion mode is 0.5 to 5 m/s and its high-speed motion mode is 4.5 to 19 m/s. The AUV model studied, as shown in Fig. 3, is connected to the dynamometer arm of the towing tank by one string, the front string is used as a model puller (attached to dynamometer) and the



FIG. 2. Towing tank of the National Iranian Marine Laboratory.

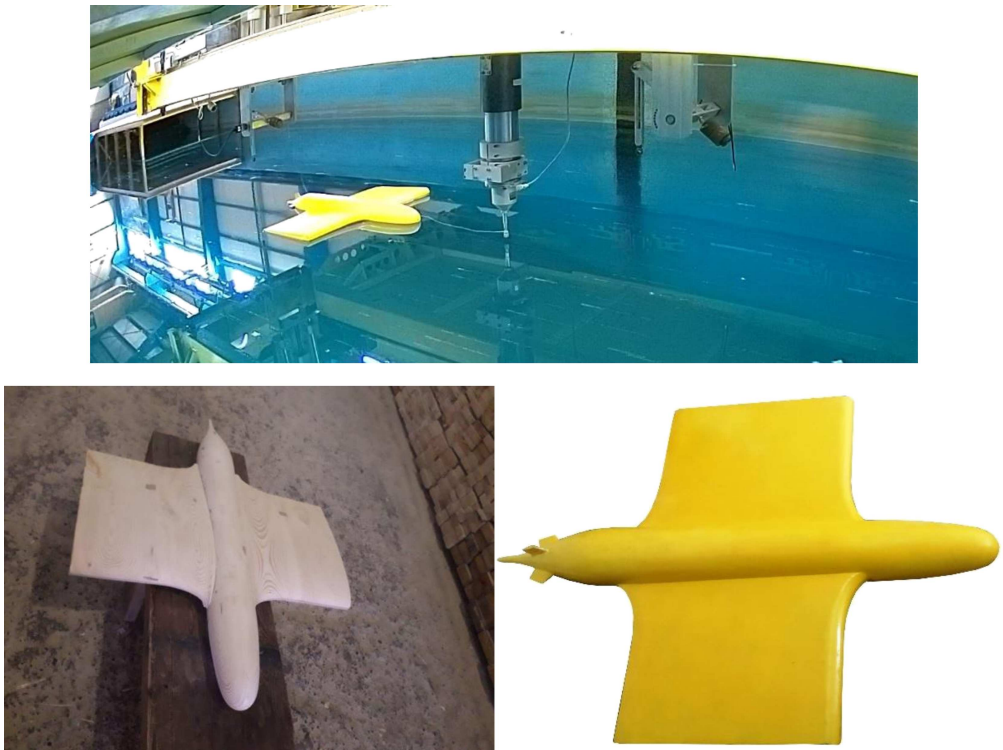


FIG. 3. Position of model, strings, dynamometer, and AUV body made of Abies wood.

end string is used as a holder and stabilizer for the motion of the used model. The AUV model is towed on the water surface at different constant speeds. At each speed, the amount of drag force experienced by the dynamometer connected to the carriage is measured. Table 2 shows the values of the test speeds and the corresponding Reynolds and Froude numbers. The characteristic length for Reynolds and Froude numbers is the vehicle length. So, we define two basic dimensionless parameters that determine flow behavior, Reynolds and Froude numbers:

$$\text{Re} = \frac{\rho V l}{\mu}, \quad (1)$$

$$\text{Fr} = \frac{V}{\sqrt{g l}}, \quad (2)$$

where V and g are velocity and gravitational acceleration respectively, l is characteristic length, and ρ and μ are fluid density and viscosity respectively.

TABLE 2. Froude and Reynolds values in model test speeds.

Velocity [m/s]	Re $\times 10^6$	Fr
0.2	0.24	0.058
0.4	0.48	0.116
0.6	0.72	0.175
0.8	0.95	0.233
1	1.2	0.291
1.2	1.4	0.35
1.4	1.67	0.408

3. NUMERICAL SIMULATION

To move the AUV model below the free surface of the water, the equations governing the continuity and air and water momentum equations must be solved. The equations for the continuity and momentum of the two-phase flow can be expressed as follows:

$$\frac{\partial}{\partial t}(\alpha_i \rho_i) + \nabla(\alpha_i \rho_i \mathbf{V}) = 0, \quad i = 1, 2, \quad (3)$$

$$\alpha_i = \frac{\nabla_i}{\nabla}, \quad i = 1, 2, \quad (4)$$

$$\sum_i \alpha_i = 1.0, \quad (5)$$

$$\sum_i \nabla \cdot (\alpha_i \mathbf{V}) = 0, \quad (6)$$

$$\frac{\partial}{\partial t} (\rho_m \mathbf{V}) + \nabla (\rho_m \mathbf{V} \otimes \mathbf{V}) = \nabla \left(-P + \mu_m \left((\nabla \mathbf{V}) + (\nabla \mathbf{V})^T \right) \right), \quad (7)$$

where \mathbf{V} is the vector of velocity and α_i is the volume fraction of phase i , \forall_i is the volume of phase i and \forall is the total volume, ρ_m and μ_m are the bulk density and viscosity of the mixture, respectively, and P is the pressure acted on the flow. Wherever there is only one phase, the volume fraction for that phase is 1, and the volume fraction for another phase is 0. Wherever the domain contains both phases, the volume fraction is between 0 and 1. The turbulence model used in this analysis is the k- ϵ standard model and the standard wall function is used as a wall function. We have chosen this model because, in the mesh used in the solution domain, due to the limitation in the computer's memory, we have encountered a limit in reducing the value of y^+ . The accuracy of the computational results is greatly influenced by the mesh density. Therefore, the first layer thickness of the boundary layer has a significant effect on the calculated results. Equation (8) can be used for an initial estimation of this thickness, denoted by Δy . And y^+ is an indicator of mesh density in the boundary layer. Variation of y^+ can be seen in Fig. 6 for $V = 1.2$ m/s. In the VOF model used, we considered water as the secondary phase and air as the primary phase. FLUENT settings in the "methods" panel for "solution methods" are: coupled algorithm is used in pressure-speed coupling, for discretizing the governing equations, least-squares cell-based algorithm is used for gradients, and PRESTO! used for pressure term, second upwind order used for momentum and turbulent kinetic energy and turbulent dissipation rate terms discretizing, compressive (spatial discretization method) is applied to discretize the volume fraction equation. Also, flow is considered as pseudo-transient.

3.1. Solution domain and boundary conditions

A three-dimensional computational cubic domain and the corresponding boundary conditions are used to simulate the surface motion of the studied AUV and are shown in Fig. 4. The model distance from the pressure inlet boundary condition is 1.2 m. This distance is common in external flow analysis. The boundary condition of the pressure outlet is also three times the relative length of the vessel, i.e., 3.6 m from the end of its tail, with zero relative pressure. The lateral boundaries are 3.72 times the total width of the AUV sides. The solution domain extended 12.86 times the maximum diameter of the AUV in

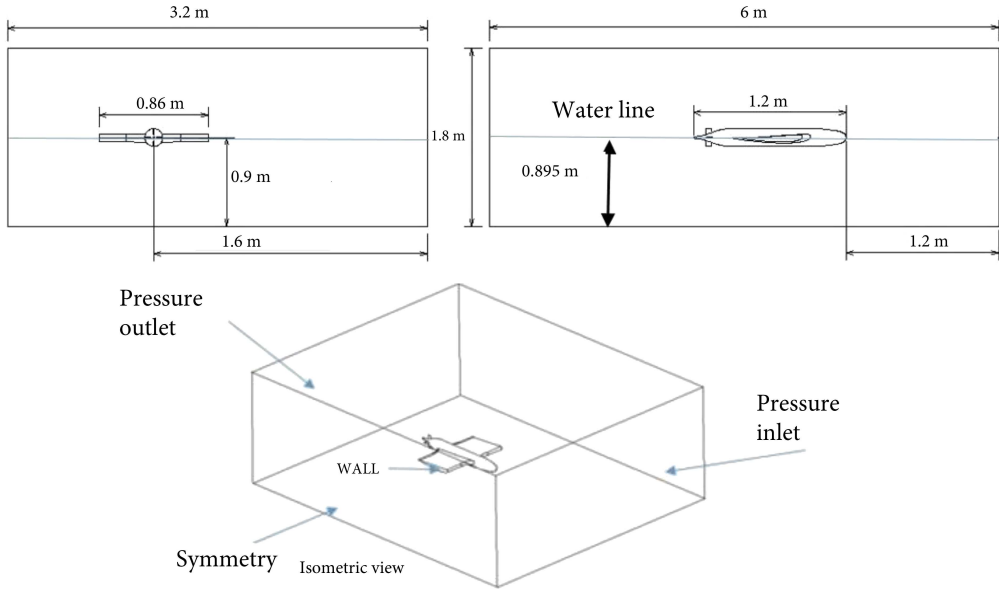


FIG. 4. Dimensions of the solution domain and determination of boundary conditions.

the direction of its diameter. The height of the domain was considered so high because our default was that the strong gradient along the height would occur. Furthermore, we consider the AUV draft in numerical analysis to be 5 mm below the longitudinal centerline, which can be seen in Fig. 4. We consider the inlet boundary to be a pressure inlet and the outlet boundary to be a pressure Outlet. Other sides of the cubic solution domain are assigned as the symmetry boundary condition. Also, the AUV model is located in the solution domain considered as a wall. This boundary condition satisfies the no-slip condition. In this study, we simulate the whole of the AUV body.

3.2. Meshing

We use a multi-block mesh to discretize the solution domain and meshing. Firstly we create a boundary layer around the model for an accurate assessment of flow features near the wall. Then, we create an unstructured mesh in the internal block of the solution domain because this type of mesh can be created easier and fast. We have discretized the rest of the solution domain so that no strong flow gradients are using structured mesh. Figure 5 depicts mesh blocks as well as boundary layer mesh. As it can be seen, we have refined the boundary layer in the areas that have more gradients. For the distance of the first computational node to the wall boundary, the range of 3.2 mm to 0.5255 mm is calculated; however, due to limitations in the processing and storage capacity of

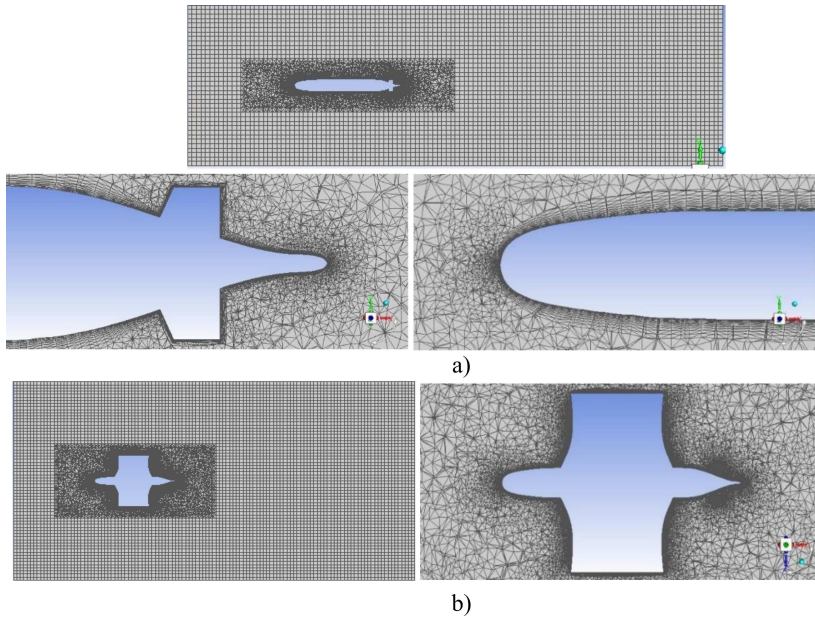


FIG. 5. Mesh and boundary layer used to solve the domain of the solution, a) X-Y, b) $Y = -0.005$ planes.

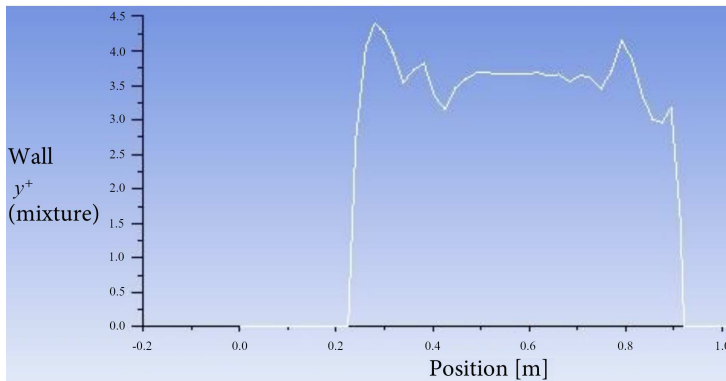


FIG. 6. y^+ variation for $V = 1.2$ m/s.

computer calculations used, we have selected the corresponding value of 1.1 mm. We also consider the growth factor of the boundary layer to be 1.2. The distance between the first computational node to the wall boundary and the thickness of the boundary layer can be calculated in the following formulas [1] and [13]:

$$\Delta y = L \Delta y^+ \sqrt{80} \text{Re}^{-(13/14)}, \quad (8)$$

$$\frac{\delta_l}{L} = \left(\frac{0.382}{\text{Re}_L^{0.2}} \right). \quad (9)$$

To demonstrate the grid independency of results, the drag coefficient (C_d) for five systematically refined meshes (from 1.2 up to 4.2 million cells) is shown in Fig. 7. After the number of meshes 1232546 (coarser mesh), the changes indicate a maximum 0.03% difference in drag coefficient by tripling the number of meshes for refining. Because this amount of refining is not cost-effective, we use the first stage mesh number, about two million (1 838 970). The experimental value at this Re is 0.018945.

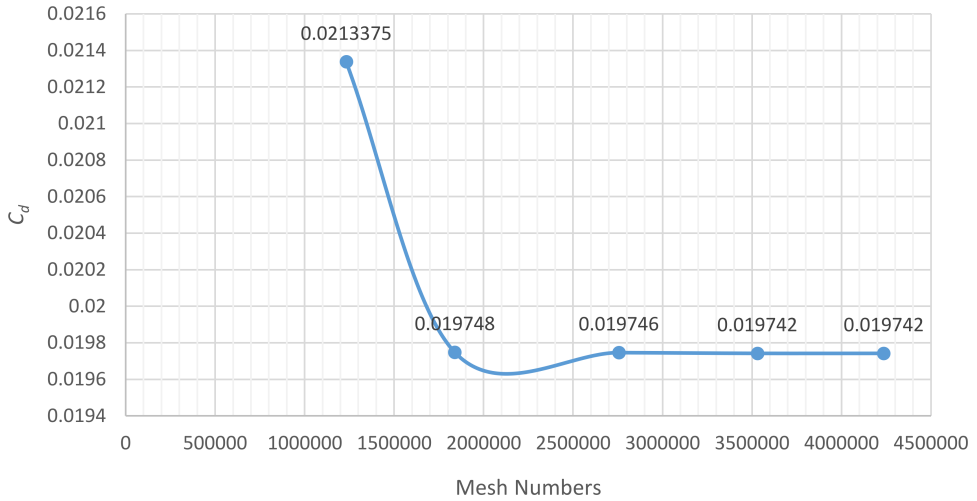


FIG. 7. C_d values related to mesh numbers (the line is interpolation graph).

4. NUMERICAL SIMULATION RESULTS

Simulation of two-phase flow around a solar AUV body to extract hydrodynamic coefficients at different speeds of AUV motion on the water surface is done by using the aforementioned domain of solution and boundary conditions. Figure 8 shows the changes in the viscosity drag coefficients (C_v) and the pressure drag coefficients (C_p) in terms of the Reynolds and Froude numbers, respectively, obtained from the CFD analysis. Definition of drag and lift coefficients (C_d and C_l) can be shown as:

$$C_d = \frac{F_d}{0.5 \times \rho \times V^2 A}, \quad (10)$$

$$C_l = \frac{F_l}{0.5 \times \rho \times V^2 A}, \quad (11)$$

where F_d and F_l are drag and lift forces, respectively, the mixture fluid bulk is defined by ρ , velocity magnitude is V , and A is wetted surface. During the AUV motion on the free surface, the wetted surface varies due to created hollows

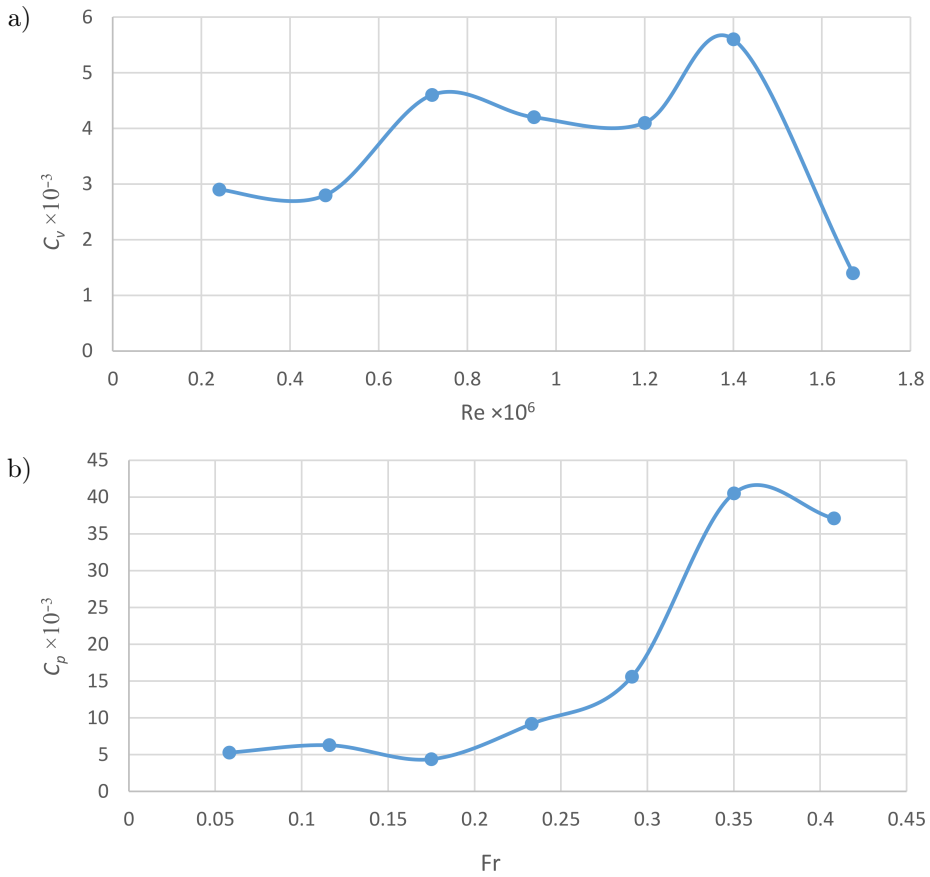


FIG. 8. Changes in viscous (a) and pressure (b) drag coefficients obtained from the CFD analysis (the line is interpolation graph).

and humps, so hydrodynamic coefficients should be averaged when reported by iterative solution in Fluent. Averaged obtained values can also be seen in Table 3.

TABLE 3. Values of pressure drag and viscosity drag coefficients according to Reynolds and Froude numbers obtained from the CFD analysis.

Fr	$Re \times 10^6$	$C_v \times 10^{-3}$	$C_p \times 10^{-3}$
0.058	0.24	2.9	5.3
0.116	0.48	2.8	6.3
0.175	0.72	4.6	4.4
0.233	0.95	4.2	9.2
0.291	1.2	4.1	15.6
0.35	1.4	5.6	40.5
0.408	1.67	1.4	37.1

As shown in Fig. 8, the viscosity drag coefficient almost increased by increasing Reynolds number until $Re = 1.4 \times 10^6$; after that, it reduced suddenly. This behavior can be observed when Reynolds number is low, flow is laminar, and therefore viscous effect is dominant. When Reynolds number increased and exceeded its critical value (e.g., $Re \geq 10^6$), separation could occur further. Although at $Re = 1.67 \times 10^6$ the wetted surface has doubled, the separation effect was greater and led to viscous drag reduction. Separation region at $Re = 1.67 \times 10^6$ is shown in Fig. 10. The pressure drag coefficient, which results from the shape resistance of the body and also includes the effect of wave-making resistance, increases with increasing Froude number. The increase in pressure drag versus the Froude number is relatively mild. However from $Fr = 0.291$ onwards, we have a significant increase in the pressure drag coefficient and this can be described with respect to the relatively short length of the vessel. It is a relatively complicated form with stagnation points on the nose and tips of wings and astern hydroplanes, and the hollows and humps interaction along the body, what creates nonlinear and unpredictable behavior. When a wave hollow formed at the nose and another formed at the tail, these two wave hollows formed a low-pressure region past the body, and the pressure drag coefficient that included wave-making drag coefficient reduced suddenly. Contrarily, for wave humps, a high-pressure region was formed and then this coefficient increased suddenly. These two humps or hollows resonate with each other. However, while a hollow formed at the nose and hump at the tail they canceled each other out. These hollows and humps can be seen in Fig. 12 by water volume fraction. Figure 9 shows the changes in the total drag coefficient with Froude numbers, and the corresponding values are shown in Table 4. These changes are similar to changes in the pressure drag coefficient, which has a predominant effect on

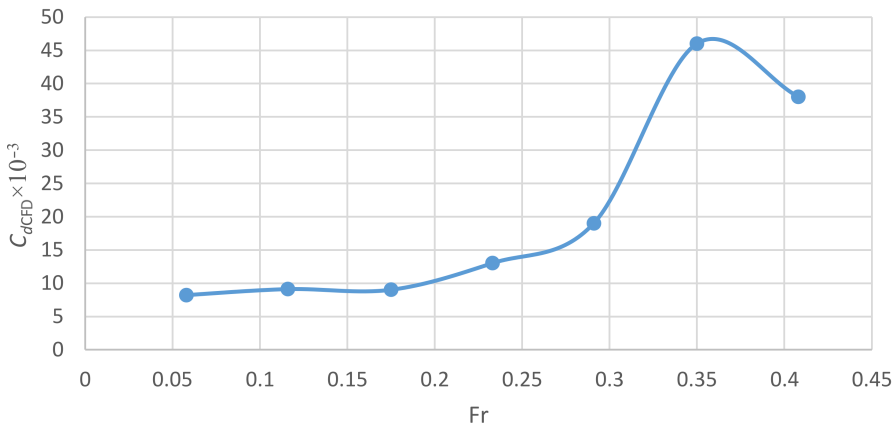


FIG. 9. Total drag coefficient variations in terms of Froude numbers, derived from the CFD analysis (the line is interpolation graph).

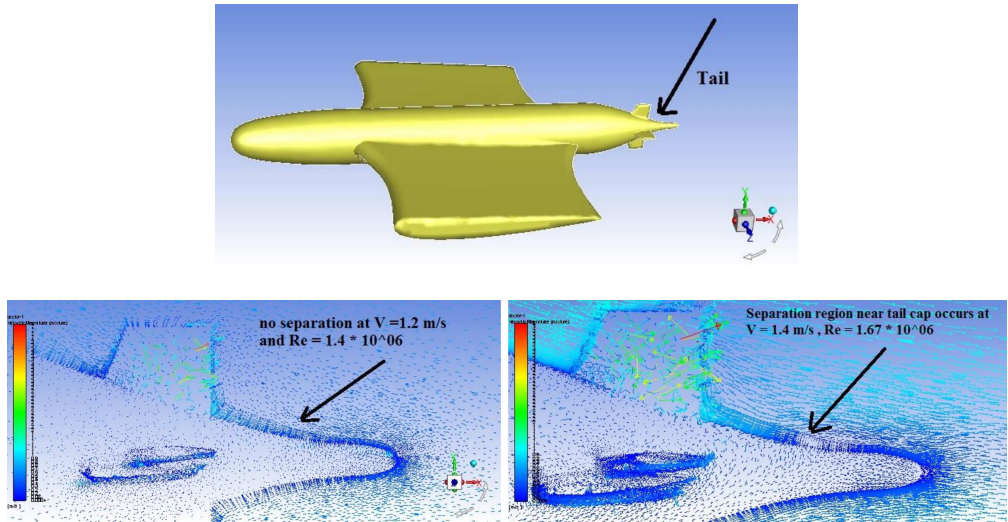


FIG. 10. Separation region near tail cap, occurs at $V = 1.4$ m/s, $Re = 1.67 \times 10^6$ and no separation at $V = 1.2$ m/s, $Re = 1.4 \times 10^6$.

TABLE 4. Total drag coefficient values in terms of Froude numbers obtained from the CFD analysis.

Fr	$C_{dCFD} \times 10^{-3}$
0.058	8.2
0.116	9.1
0.175	9
0.233	13
0.291	19
0.35	46
0.408	38

surface motion. The same incremental behavior can be seen in this diagram for the same reason mentioned above. Also, it is notable that these obtained drag coefficients included individual components drag and induced drag due to foils sections of wings and rudders. The applied turbulence model considered these effects (induced drag and eddies formed due to foils sections).

The wave patterns formed on a plane that is $\alpha = 0.5$ on the AUV body can be seen in Fig. 11 compared to the photographs taken from the film submitted from the laboratory during the test. These patterns are presented for different velocities. In the figures obtained from the CFD results, the volume fraction of water is shown. The green color refers to the areas where the volume fraction of water is equal to 0.5. As you can see in Fig. 11, the significant part of AUV

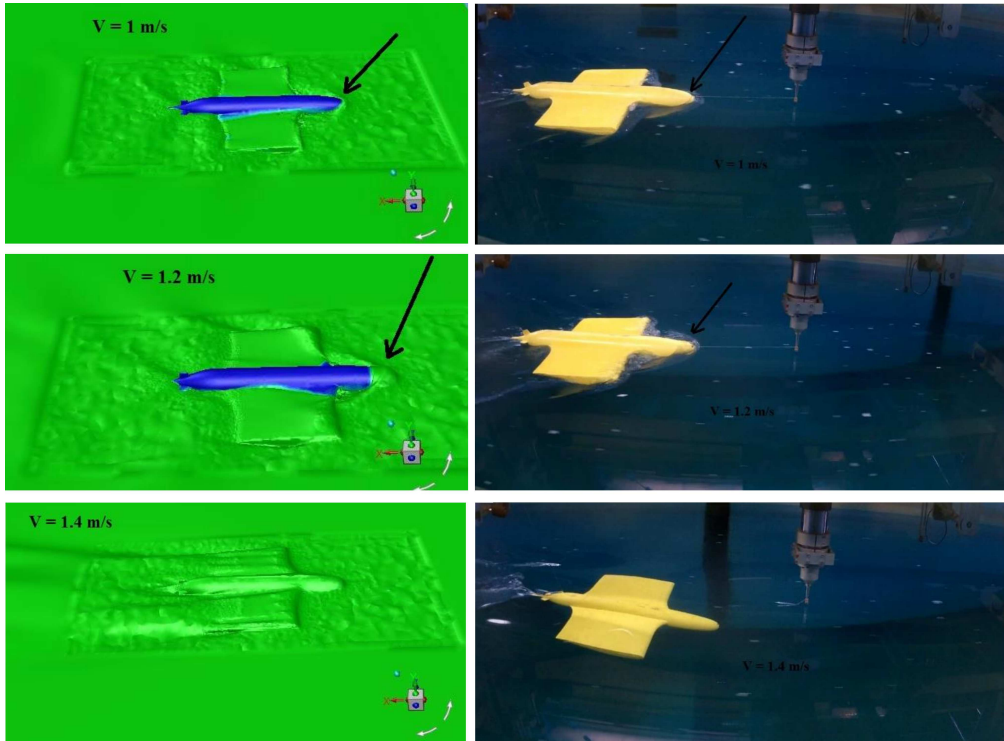


FIG. 11. Comparison between the wave pattern formed on the AUV body and its surroundings in the CFD analysis and experimental results on the surface that is $\alpha = 0.5$.

body sinks at a velocity of 1.2 m/s and the whole body sinks at a speed of 1.4 m/s. Figure 12 also depicts wave patterns formed on the AUV body at two velocities and at the nose in all test velocities in CFD, indicated by α contour for the velocities that AUV towed on the water surface.

The lift coefficient changes in the CFD analysis are presented in Fig. 13 and Table 5. Due to the large wings where the photovoltaic panels are installed, the amount of lift force created is significant. As can be seen from the values in Table 5 and in Fig. 13, with increasing Froude numbers, the lift force sign is initially positive, then it becomes negative and its numerical value increases sharply. This trend of sharp increase in its numerical value is visible at the Froude number equal to 0.175, and the large wing is not submerged in water. Therefore, the water flow is in contact with the lower part of the large wing, which is from the NACA0015 section, leading a positive lift force production. However, since then, two large wings have been submerged, and due to the smooth and asymmetrical surface of the upper surface of the wing, the negative lift force is produced and as the Froude number increased, the absolute value of this force increased.

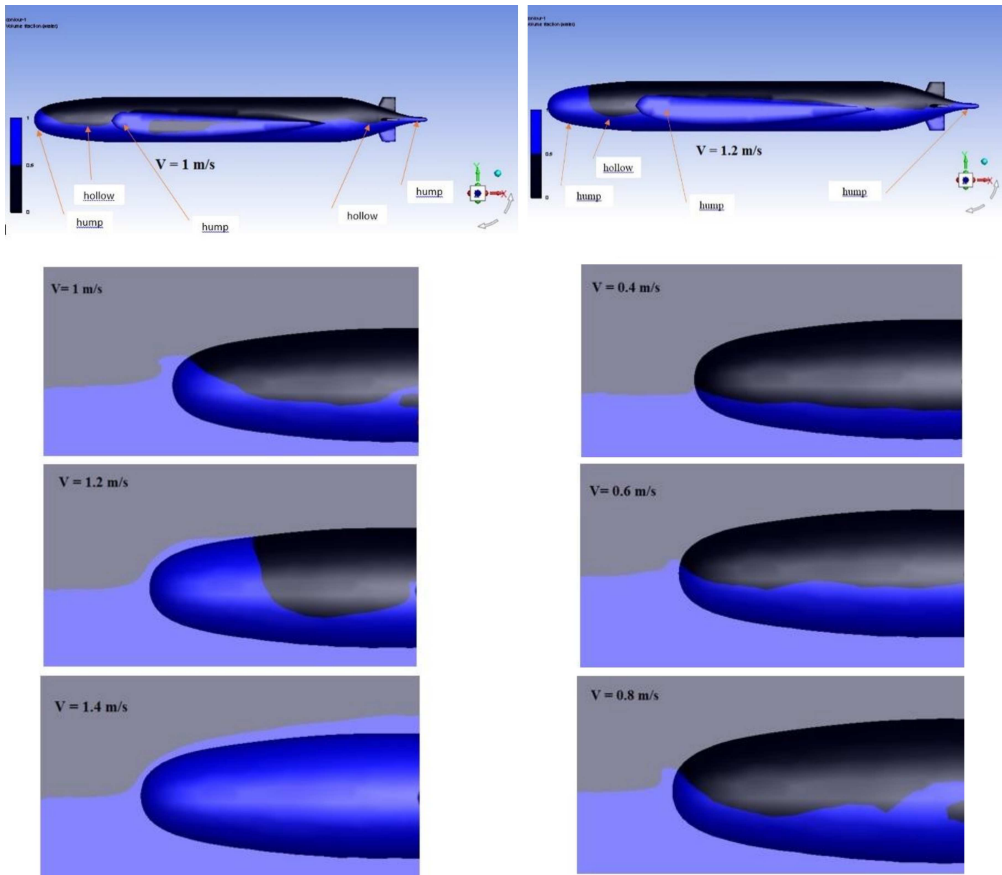


FIG. 12. Wave pattern formed on the AUV nose and hull (at $Re = 1.2, 1.4 \times 10^6$) in CFD, indicated by α contour, hollows and humps can be seen along the nose at each velocity.

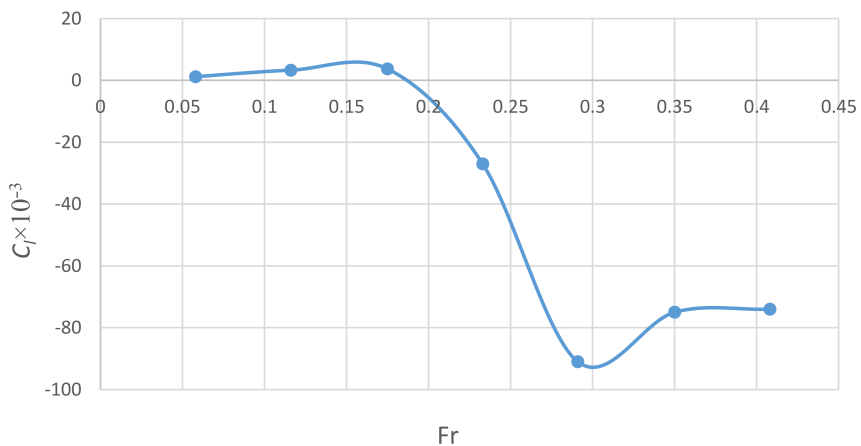


FIG. 13. Lift coefficient changes according to Froude numbers obtained from the CFD analysis (the line is interpolation graph).

TABLE 5. Lift force coefficients according to Froude numbers, obtained from the CFD analysis.

Fr	$C_l \times 10^{-3}$
0.058	1.2
0.116	3.3
0.175	3.7
0.233	-27
0.291	-91
0.35	-75
0.408	-74

Figure 14 shows a comparison between the drag coefficient obtained from the CFD analysis and laboratory results. The wet surface area for the AUV motion when the vessel is not submerged is 0.58115 m^2 , and when the vessel is completely submerged, it is doubled. Table 6 presents the values of these two types of results, and Table 7 shows the deviation values of the numerical solution results from the laboratory results as the percentage of deviation in Froude numbers terms. The relation (12) indicates this error obtained in the procedure. The maximum error value is 13.4%. This can be due to uncertainties in the construction of the model, calibration of the dynamometer, and especially the amount of variable AUV water draft during the submersion in the water during the test, as well as mesh errors in the zone of the unstructured mesh, which can lead to errors in the diffusion term and affect the value of the drag coefficient.

$$\text{Error} = \frac{\text{CFD values} - \text{Exp values}}{\text{Exp values}} \times 100. \quad (12)$$

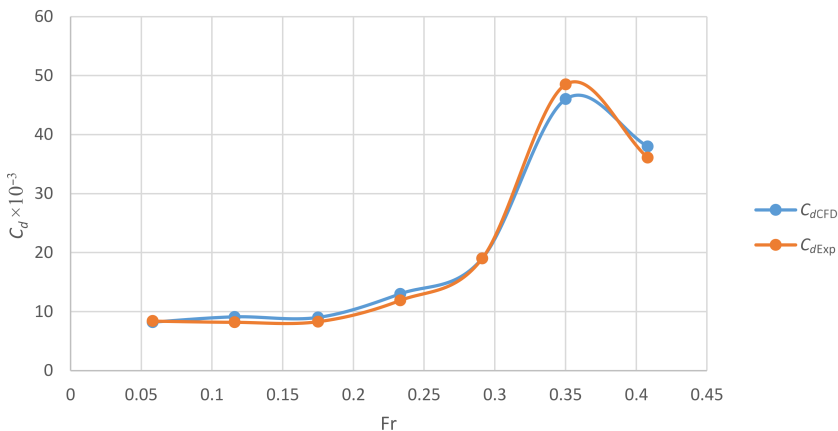


FIG. 14. Comparison between drag coefficients from laboratory results (C_{dEXP}) and CFD results (C_{dCFD}) (blue and orange line are interpolation graphs).

TABLE 6. Drag coefficients obtained from the CFD analysis and laboratory results.

Fr	$C_{dExp} \times 10^{-3}$	$C_{dCFD} \times 10^{-3}$
0.058	8.4	8.2
0.116	8.2	9.1
0.175	8.3	9
0.233	11.9	13
0.291	19	19
0.35	48.5	46
0.408	36.1	38

TABLE 7. Deviation values of drag coefficient, obtained from numerical solution concerning laboratory results according to Froude numbers.

Fr	0.058	0.116	0.175	0.233	0.291	0.35	0.408
Error [%]	2.1	10.6	9.3	13.4	4.3	4.9	6.7

Figure 15 and Table 8 show the values of drag force obtained from the CFD analysis and laboratory data.

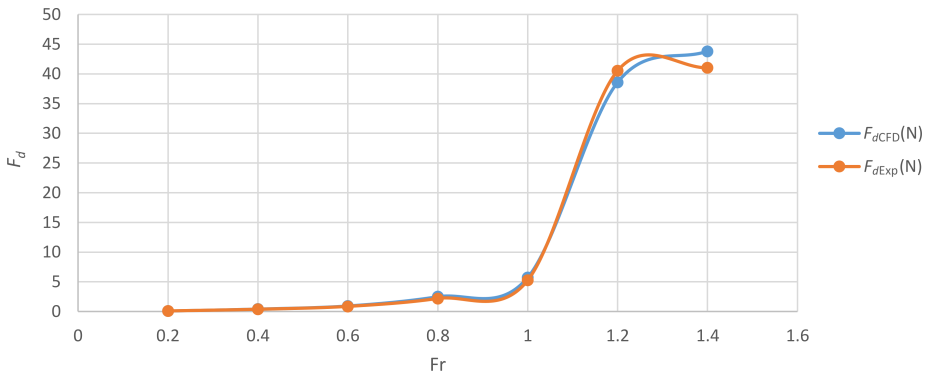


FIG. 15. Comparison of drag force values obtained from CFD with experimental data (blue and orange line are interpolation graphs).

TABLE 8. Drag force values obtained from CFD analysis and laboratory data.

V [m/s]	F_{dExp} (N)	F_{dCFD} (N)
0.2	0.098	0.096
0.4	0.38	0.42
0.6	0.86	0.94
0.8	2.20	2.5
1	5.25	5.72
1.2	40.54	38.56
1.4	41.05	43.8

5. CONCLUSION

To estimate the hydrodynamic forces applied to a solar AUV in surface motion mode, a 1:1 scale model was made of Abies wood and it was tested in the towing tank of the National Iranian Marine Laboratory. The values, including wave patterns formed on and around the body obtained from this experiment for validation, were also analyzed numerically. ANSYS FLUENT 18 commercial code was used in the numerical analysis. It was observed that at a velocity of 1.2 m/s, the significant part of vessel was submerged and at a velocity of 1.4 m/s it was completely submerged. This can be seen in both experimental and CFD analysis contours. Increasing the amount of the wet surface from 1.2 m/s leads to an increase in the amount of drag force. Comparing the results of numerical solutions with laboratory data, the maximum error of 13.4% is observed in Reynolds number close to 10^6 . Uncertainties in the construction and testing of the model, the limited computer memory used for numerical analysis to make the mesh or boundary layer more refined as well as mesh errors can be the causes of such errors. The maximum drag value of 43.8 N in numerical analysis and 41.054 N in the model test, at a velocity of 1.4 m/s, indicates the maximum power consumption of 61.32 W. If two 50 W panels are used, the required power can be provided. Besides, by changing the lift coefficient, we also face an increment similar to the growth of the drag coefficient in terms of Reynolds number. However, the lift coefficient is negative in terms of the velocity at which the large wings submerged in the water. This is due to the asymmetry of the upper surface of the large wing relative to its lower surface. The installation of photovoltaic panels on wings was permitted by cutting off the upper surface of the large wing along the chord, and this created a horizontal line along the wing cross-section. While the large wing was submerged, by increasing the velocity, flow pressure on the upper surface became higher than on the lower surface. This led to a negative and downward lift.

This study focused on the possibility to use solar energy to provide the power required by a solar AUV. The case of AUV motion in this study was analyzed for the vessel moving on the water surface and at the same time receiving solar energy. In future research, we will test the AUV underwater motion, which is independent of the free surface effect.

REFERENCES

1. ANSYS CFX Release 12.1, ANSYS, Inc., Canonsburg, PA, USA, 2009.
2. De Marco A., Mancini S., Miranda S., Scognamiglio R., Vitiello L., Experimental and numerical hydrodynamic analysis of a stepped planing hull, *Applied Ocean Research*, **64**: 135–154, 2017.

3. Javadi M., Dehghan Manshadi M., Kheradmand S., Moonesun M., Experimental investigation of the effect of bow profiles on resistance of an underwater vehicle in free surface motion, *Journal of Marine Science and Application*, **14**(01): 53–60, 2015.
4. Rhee K., Choi J., Lee S., Mathematical model of wave forces for the depth control of a submerged body near the free surface, The Eighteenth International Offshore and Polar Engineering Conference, 6–11 July, Vancouver, Canada, 2008.
5. Mansoorzadeh Sh., Javanmard E., An investigation of free surface effects on drag and lift coefficients of an autonomous underwater vehicle (AUV) using computational and experimental fluid dynamics methods, *Journal of Fluids and Structures*, **51**: 161–171, 2014.
6. Moonesun M., Ghasemzadeh F., Korol Y., Nikrasov V., Yastreba A., Ursolov A., Mahdian A., Technical notes on the near surface experiments of submerged submarine, *International Journal of Maritime Technology*, **5**: 41–54, 2016.
7. Dalayeli H., Javadi M., Mousavizadegan S.H., Gharachahi A., Moonesun M., Ursalov A., Wave profile and deck wetness of submarine at surface condition, *International Journal of Recent Advances in Multidisciplinary Research*, **2**(12): 1083–1091, 2015.
8. Moonesun M., Korol Y.M., Moosavizadegan S.H., Dalayeli H., Mahdian A., Javadi M., Brazhko A., Wave making system in submarines at surface condition, *Indian Journal of Geo Marine Sciences*, **45**(1): 44–53, 2016.
9. Moonesun M., Ghasemzadeh F., Korol Y., Valeri M., Yastreba A., Ursalov A., Effective depth of regular wave on submerged submarines and AUVs, *International Robotics & Automation Journal*, **2**(6): 208–216, 2017.
10. Nematollahi A., Dadvand A., Dawoodian M., An axisymmetric underwater vehicle-free surface interaction: A numerical study, *Ocean Engineering*, **96**: 205–214, 2015.
11. Razgallah I., Kaidi S., Smaoui H., Sergeant Ph., The impact of free surface modelling on hydrodynamic forces for ship navigating in inland waterways: water depth, drift angle, and ship speed effect, *Journal of Marine Science and Technology*, **24**: 620–641, 2019.
12. Salari M., Rava A., Numerical investigation of hydrodynamic flow over an AUV moving in the water-surface vicinity considering the laminar-turbulent transition, *Journal of Marine Science and Application*, **16**: 298–304, 2017.
13. Shariati S.K., Mousavizadegan S.H., The effect of appendages on the hydrodynamic characteristics of an underwater vehicle near the free surface, *Applied Ocean Research*, **67**: 31–43, 2017.
14. Steenson L.V., Phillips A.B., Furlong M.E., Rogers E., Turnock S.R., The performance of vertical tunnel thrusters on an autonomous underwater vehicle operating near the free surface in waves, Second International Symposium on Marine Propulsors SMP'11, Hamburg, Germany, June 2011.

Received August 28, 2020; revised version December 28, 2020.